CT-guided spatial normalization of nuclear hybrid imaging adapted to enlarged ventricles: Impact on striatal uptake quantification

Alae Eddine El Barkaoui, Christian Scheiber, Thomas Grenier, Marc Janier, Anthime Flaus

NeuroImage 294 (2024) 120631

Contents lists available at ScienceDirect

NeuroImage

journal homepage: www.elsevier.com/locate/ynimg

CT-guided spatial normalization of nuclear hybrid imaging adapted to enlarged ventricles: Impact on striatal uptake quantification

Alae Eddine El Barkaoui [a,b], Christian Scheiber [a,c], Thomas Grenier [b], Marc Janier [a,d,e], Anthime Flaus [a,d,f,*]

[a] Département de médecine nucléaire, Groupement Hospitalier Est, Hospices Civils de Lyon, Bron, France
[b] INSA-Lyon, Universite Claude Bernard Lyon 1, CNRS, Inserm, CREATIS UMR 5220, U1294, F-69100, LYON, France
[c] Institut des Sciences Cognitives Marc Jeannerod, UMR 5229, CNRS, CRNL, Université Claude Bernard Lyon 1, Lyon, France
[d] Faculté de Médecine Lyon Est, Université Claude Bernard Lyon 1, Lyon, France
[e] Laboratoire d'Automatique, de génie des procédés et de génie pharmaceutique, LAGEPP, UMR 5007 UCBL1 – CNRS, Lyon, France
[f] Centre de Recherche en Neurosciences de Lyon, INSERM U1028/CNRS UMR5292, Lyon, France

ARTICLE INFO

Keywords:
Normalization
Large ventricles
Tissue probability maps
Brain template
Aging
Quantification

ABSTRACT

Introduction: Spatial normalization is a prerequisite step for the quantitative analysis of SPECT or PET brain images using volume-of-interest (VOI) template or voxel-based analysis. MRI-guided spatial normalization is the gold standard, but the wide use of PET/CT or SPECT/CT in routine clinical practice makes CT-guided spatial normalization a necessary alternative. Ventricular enlargement is observed with aging, and it hampers the spatial normalization of the lateral ventricles and striatal regions, limiting their analysis. The aim of the present study was to propose a robust spatial normalization method based on CT scans that takes into account features of the aging brain to reduce bias in the CT-guided striatal analysis of SPECT images.

Methods: We propose an enhanced CT-guided spatial normalization pipeline based on SPM12. Performance of the proposed pipeline was assessed on visually normal [^{123}I]-FP-CIT SPECT/CT images. SPM12 default CT-guided spatial normalization was used as reference method. The metrics assessed were the overlap between the spatially normalized lateral ventricles and caudate/putamen VOIs, and the computation of caudate and putamen specific binding ratios (SBR).

Results: In total 231 subjects (mean age ± SD = 61.9 ± 15.5 years) were included in the statistical analysis. The mean overlap between the spatially normalized lateral ventricles of subjects and the caudate VOI and the mean SBR of caudate were respectively 38.40 % (± SD = 19.48 %) of the VOI and 1.77 (± 0.79) when performing SPM12 default spatial normalization. The mean overlap decreased to 9.13 % (± SD = 1.41 %, $P < 0.001$) of the VOI and the SBR of caudate increased to 2.38 (± 0.51, $P < 0.0001$) when performing the proposed pipeline. Spatially normalized lateral ventricles did not overlap with putamen VOI using either method. The mean putamen SBR value derived from the proposed spatial normalization (2.75 ± 0.54) was not significantly different from that derived from the default SPM12 spatial normalization (2.83 ± 0.52, $P > 0.05$).

Conclusion: The automatic CT-guided spatial normalization used herein led to a less biased spatial normalization of SPECT images, hence an improved semi-quantitative analysis. The proposed pipeline could be implemented in clinical routine to perform a more robust SBR computation using hybrid imaging.

Abbreviation: VOI, volume of interest; SD, standard deviation; SBR, specific binding ratio; MNI, Montreal Neurological Institute; TPM, tissue probability map; SPM, statistical parametric mapping; LVV, lateral ventricular volume; [^{123}I]-FP-CIT, 123- radiolabeled 2β-carbomethoxy-3β-(4-iodophenyl)-N-(3-fluoropropyl) nortropane; CSF, cerebrospinal fluid; GM, gray matter; WM, white matter; MIITRA, Multichannel Illinois Institute of Technology & Rush University Aging; ICBM, International Consortium for Brain Mapping; NMI, normalized mutual information; IQR, interquartile range (IQR); SE, standard error.

* Corresponding author at: Département de médecine nucléaire, Groupement Hospitalier Est, Hospices Civils de Lyon, Bron, France.
E-mail address: anthime.flaus@chu-lyon.fr (A. Flaus).

https://doi.org/10.1016/j.neuroimage.2024.120631
Received 9 December 2023; Received in revised form 25 April 2024; Accepted 30 April 2024
Available online 1 May 2024

1. Introduction

Numerous neurological studies aim to perform quantitative analyses of positron emission tomography (PET) or single-photon emission computed tomography (SPECT) images by using VOI template or voxel-based analysis. In both cases, this requires putting images in the same anatomical space, defined by a population average, also known as a template. Standard reference frames have been established to consistently and accurately assess inter-subject anatomical correspondences in images (e.g., the stereotactic space of the Montreal Neurological Institute, MNI (Brett et al., 2002; Martino et al., 2013). This process is known as spatial normalization or registration and allows regions that are pre-defined on the templates to be overlaid on the spatially registered image, allowing automatic identification of different structures. An inaccurate spatial normalization can lead to remarkable anatomical mismatches, leading to biased quantification and reduced diagnostic effectiveness (Della Rosa et al., 2014; Zhang et al., 2022). By way of illustration, in studies involving dopamine transporter scintigraphy (123- radiolabeled 2β-carbomethoxy-3β-(4-iodophenyl)-N-(3--fluoropropyl) nortropane; [^{123}I]-FP-CIT or Technetium-99m labeled tropane derivative; ^{99m}Tc-TRODAT-1), the spatial normalization accuracy will determine the accuracy of striatal uptake specific binding ratio (SBR) measurements.

Spatial normalization can be based on functional images (SPECT or PET) or anatomical images (computed tomography, CT, or magnetic resonance imaging, MRI). For example, in studies involving dopamine transporter scintigraphy, SPECT or PET-guided spatial normalization are very sensitive to both specific and non-specific ligand binding (Kim et al., 2015). CT or MRI-based spatial normalization are not affected by this as they work independently from transporter density and provide anatomical information that is relevant for the warping process. MRI is the reference for SPECT or PET brain image spatial normalization, however the improvement of the image quality of CT scanners and the growing widespread use of hybrid imaging devices combining SPECT and CT, or PET and CT, makes CT-guided spatial normalization a more practical alternative. The feasibility of CT-guided spatial normalization has been reported, however it is complicated by the significant differences in skull, brain tissue, and air intensities as popular cost-functions applied to CT images are primarily driven by the contrast of air and bone while soft tissues have relatively equivalent similarity metrics (Carmichael et al., 2007; Rorden et al., 2012; Kim et al., 2015; Matsuda et al., 2021).

Well-established algorithms for structurally guided and atlas-based spatial normalization use a combined approach for segmentation and normalization, in a single probabilistic framework (Fischl et al., 2004; Ashburner and Friston 2005). For this, tissue probability maps (TPMs), which represent the prior probability of different tissue classes being found at each location in an image, are indispensable (Ashburner and Friston 2005). Templates and their associated TPMs are constructed from MRI of numerous brains that are registered into a common space and are used for spatial normalization of MRI and CT images. This unified framework is implemented in the widely used Statistical Parametric Mapping (SPM) software (Wellcome Trust Centre for Neuroimaging, London, UK), and has been successfully used in numerous investigations (Allen et al., 2008; Colloby et al., 2011; Izquierdo-Garcia et al., 2014). Another approach for non-linear deformations relies on deep neural networks to learn the spatial normalization function (Dalca et al., 2019; Krebs et al., 2019), but this either requires some sort of prior image processing or it is restricted to MR imaging.

Templates and TPMs are representative of an age specific group of individuals, usually young adults, from which they are generated. The substantial inter-individual variability in brain images with ventricular enlargement due to age-related atrophy, pathological atrophy or hydrocephalus, poses significant challenges in the delineation of adequate TPMs. These challenges result in a poor segmentation, especially of lateral ventricles, hence a less accurate spatial normalization (Allen et al., 2008; Kennedy et al., 2009; Peelle et al., 2012; Eloyan et al., 2014;) and biased metabolic activity measurements (Reig et al., 2007). In this context, there is a consensus that the performance of default structure-guided spatial normalization in SPM12 is impacted when dealing with ventricular enlargement (Ganzetti et al., 2018). Moreover, accurate delineation of striatal structures that are adjacent to the lateral ventricles remains challenging (Makowski et al., 2018). As a result, measurements of radiotracer uptake could be biased (Reig et al., 2007). Therefore, new tissue priors were developed, and were generated from individuals with ages similar to what is commonly seen in neurodegenerative studies, and the delineation of subcortical structures was improved to compensate age-related bias in tissue classification (Lorio et al., 2016; Ridwan et al., 2021; Niaz et al., 2022).

The purpose of the present study was twofold: to propose a more robust CT-guided spatial normalization method with features to deal with CT scans and the hallmarks of the aging brain and to compare the proposed pipeline with the default SPM12 CT-guided spatial normalization pipeline. The comparison of the two pipelines relied on, first, the assessment of the performance of the lateral ventricles' spatial normalization, and second, the impact on the semi-quantification of [^{123}I]-FP-CIT images from subjects with uncertain parkinsonian syndromes and visually normal scans.

2. Methods

2.1. Subjects, system data acquisition, and reconstruction

[^{123}I]-FP-CIT SPECT/CT images were acquired at Hospices Civils de Lyon nuclear medicine department between 2008 and 2017 and described in the study reported by Fahmi et al. (2020). We included 237 subjects (117 women and 120 men) with uncertain parkinsonian syndromes, visually normal [^{123}I]-FP-CIT SPECT images and without any brain injury (tumors or stroke); the age of whom ranged from 16 to 88 years (mean ± standard deviation (SD) = 62.2 ± 15.7 years). Clinical indications for obtaining a diagnostic CT scan were given in all cases. These subjects were representative of routine clinical practice at our site. Imaging was performed using a Symbia® T2 (Siemens Healthineers, Erlangen, Germany) system equipped with low energy high-resolution collimators. The CT scanning parameters were held constant in the helical scanning mode: pitch = 1, 130 kV, 150mAs, reconstruction matrix = 512 × 512, voxel size = 0.59 mm × 0.59 mm × 1.5 mm. The CT acquisition protocol resulted in a volumetric dose index of 35 mGy, a mean effective dose of 1.64 ± 0.15 mSv, while the mean dose length product was 940 ± 179.95 mGy*cm. The SPECT scanning parameters were held in circular step and shoot mode: 120 projection angles over 360° (each projection lasted 30 s), hardware zoom = 1.23 × 1.23, in-plane pixel size = 3.9 mm by 3.9 mm, slice thickness = 3.9 mm, reconstruction matrix = 128 × 128, photo peak imaging window = 159 keV ± 8 %, and acquisition time = 30 min. The mean injected dose of [^{123}I]-FP-CIT was 185.97 ± 14.17 MBq (range 158–211 MBq), and the image acquisition started 3 h after the injection. Images were reconstructed using a commercial 3-dimensional ordered subset expectation maximization algorithm (Flash3D®; Siemens Healthineers) with 10 iterations, 8 subsets. Attenuation correction relied on μ-map derived from the down sampled CT and scatter correction used a triple energy window method. Images were smoothed using a Gaussian filter with an 8 mm full-width-at-half-maximum. A visual check was conducted to verify the alignment between the CT and SPECT images in the native space. The datasets generated and/or analyzed during the current study are not publicly available due to institutional restrictions on patient confidentiality, prior consent, and privacy.

2.2. Methods description

We hypothesized that performing a custom pipeline for the CT-guided anatomical standardization that is more robust for dealing

with low dynamic ranges of soft tissue in CT scans and more suitable to the aging brain anatomy could reduce spatial normalization errors. This can reduce the overlap differences between the spatially normalized lateral ventricles and the striatal VOIs of the reference space. Thus, we compared SPM12 default spatial normalization with the proposed spatial normalization pipeline. The workflow of the proposed pipeline is fully automated and relies on tools available in SPM12. All programs were developed using MATLAB (R2021a; The MathWorks Inc., Natick, MA, USA).

2.2.1. Estimating lateral ventricular volumes within the cohort

The estimation of LVVs before and after warping is a robust metric to evaluate the spatial normalization performance on the adjacent striatal regions. This is explained by the fact that the size of the spatially normalized lateral ventricles and the adjacent striatal regions should match those of the template after the warping.

The LVV estimation pipeline consisted of two steps. Firstly, we segmented the cerebrospinal fluid (CSF) using SPM12 dedicated segmentation tools; and secondly, we extracted the lateral ventricles from the CSF (Fig. 1). In the 1st step, we used 6 TPMs combined with adapted segmentation parameters (Table 1). Six tissue classes were then generated from the CT image: white matter (WM), gray matter (GM), CSF, skull, soft tissue, and air. To compensate for the effect of the spatial normalization (volumetric changes induced by non-rigid deformations), volume information at each voxel is conserved by multiplying tissue density values by the Jacobian determinant. In the 2nd step, we used the binary mask that is part of the Automatic Lateral Ventricle delIneatioN (ALVIN) program (Kempton et al., 2011), with the aim of excluding CSF outside the lateral ventricles (superior cistern, sulcal CSF, and the third ventricle). This mask takes into consideration the large inter-subject variability in the shape and the size of lateral ventricles that may still exist even after the spatial normalization.

In the case of a severe lateral ventricular enlargement, segmentation of CSF using the 'Segmentation' module of SPM12 may fail and produce unreliable volume measurement. We therefore used an additional segmentation technique based on thresholding and masking (using the same mask). In case of large differences in LVV estimations between the two segmentation techniques (> mean difference [mL] + 1 SD), images were analyzed visually to detect severe lateral ventricular enlargement (potential hydrocephalus) that caused spatial normalization failure. These cases were excluded from the analysis.

The algorithm works with a parametrization of the image intensities for each tissue type using a Gaussian Mixture Model. For CT images, a non-parametric approach (NP) was used to model the tissue intensities of white matter (WM), gray matter (GM), cerebrospinal fluid (CSF), skull, soft tissue, and air

Table 1
Settings for the unified segmentation algorithm.

Setting	Parameter	CT
Bias field correction	Full width at half maximum	Disabled
	Regularization	-
Approach for modeling tissue intensities	GM	NP
	WM	NP
	CSF	NP
	Bone	NP
	Tissue	NP
	Air	NP
Warping regularization	Absolute displacement	0
	Membrane energy	0.001
	Bending energy	0.5
	Linear elasticity 1	0.05
	Linear elasticity 2	0.2

2.2.2. Spatial normalization pipeline

Before conducting the spatial normalization of CT images and applying the generated deformation fields to the SPECT images, the 1st step of the proposed pipeline consisted of using a rigid body model to align CT and SPECT images of each subject, using the 'Coregister' module of SPM12. This step was intended to remove any unexpected misalignment (incorrect system calibration or head motion between SPECT and CT acquisitions). The chosen fixed image for spatial normalization was the CT image, while the moved one was the SPECT image (Fig. 3). The transformation was parameterized by three translations and three rotations around each axis. Subsequently, the intention was to estimate the transformation, by finding parameters that optimize the objective function. In the present case of multimodal images, the chosen similarity measure was intensity based, and relied on normalized mutual information (NMI) computed as:

$$\mathrm{SM}\ (\mathrm{C},\mathrm{S}) = \frac{\mathrm{H(C)} + \mathrm{H(S)}}{\mathrm{H(C,S)}} \tag{1}$$

Where H (C) and H (S) are the marginal entropies of the CT and SPECT images respectively, and H (C, S) is the joint entropy of C and S and were computed as:

$$\mathrm{H}\ (\mathrm{C}) = -\sum_{c\in C} p\{c\}\log(p\{c\}) \tag{2}$$

$$\mathrm{H}\ (\mathrm{S}) = -\sum_{s\in S} p\{s\}\log(p\{s\}) \tag{3}$$

$$\mathrm{H}\ (\mathrm{C},\mathrm{S}) = -\sum_{c\in C}\sum_{s\in S} p\{c,s\}\log(p\{c,s\}) \tag{4}$$

Where c and s are the set of values occurring in CT and SPECT images respectively, p{c} and p{s} are the marginal probabilities of c and s respectively and p{c,s} the joint distribution of c and s.

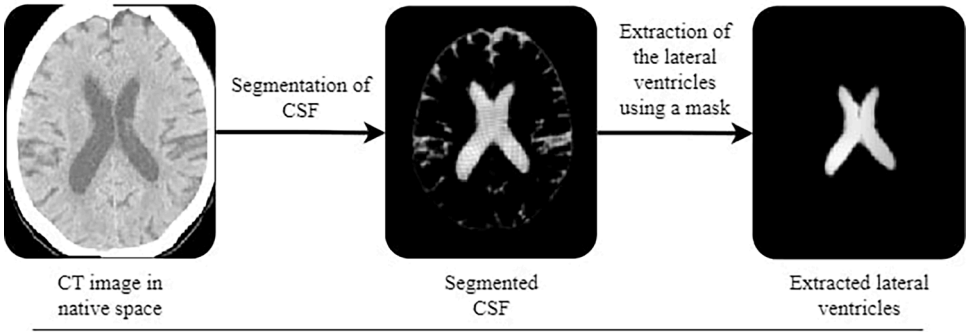

Fig. 1. Pipeline of the lateral ventricles' segmentation. The cerebrospinal fluid (CSF) was segmented using SPM12 and a binary mask was then applied. In the output, we obtained a 3D image of the lateral ventricles.

The goal of using NMI was to overcome the sensitivity of mutual information to variations of the overlap size between the fixed image and the moved one. While being written in the new space, the images were sampled using 4th° B-spline interpolation and smoothed slightly as was the histogram.

In the 2nd step of the proposed pipeline (Fig. 3), the intensity of CT images was converted to the image brightness range of a CT template (Rorden et al., 2012). This intensity transformation was intended to increase the intensity range representing the CSF and brain tissue and reduce intensity contrast between the latter and the skull. The intensity-transformed CT images were then subject to a non-rigid transformation with the CT template using the 'Old Normalization' module of SPM12. This step was intended to ease the execution of the unified framework of the 2nd non-rigid registration (the 3rd step of the pipeline), by providing reasonable starting estimates for the local optimization procedure. In other words, the primary aim of this spatial registration step was to compensate partially for potentially enlarged ventricles. The used enhanced CT template (Rorden et al., 2012) was adapted to common spatial normalization cost functions (such as least-squares) and was generated from healthy older subjects (mean age $\pm$ SD = 61.3 $\pm$ 18.4 years). The LVV of this CT template was 40.98 mL. Within this registration step, an affine registration (involving 12-parameter affine transformation) was followed by estimating nonlinear deformations, defined by a linear combination of 3D discrete cosine transform (DCT). The matching between the CT image and the CT template involved minimizing the membrane energies of the deformation fields and the residual squared difference (Ashburner et al., 2021).

In the 3rd step of the proposed pipeline (Fig. 3), we implemented an image-processing step using the unified normalization segmentation within the 'Segmentation' module found in SPM12. A different set of TPMs were used (Ridwan et al., 2021) as compared to SPM12 default normalization pipeline. Indeed, both the standard template image and TPMs found in SPM12 are based on MRI T1-weighted data from 152 young normal adults (age range: 18–44 years, International Consortium for Brain Mapping [ICBM152] template). Thus, after the spatial normalization, age-related enlarged lateral ventricles tend to be misaligned and the LVV does not match that of the ICBM152 template (Ganzetti et al., 2018). The comprehensive older adult brain atlas, Multichannel Illinois Institute of Technology & Rush university Aging (MIITRA), contains a T1-weighted template and TPMs based on 222 older adults (age range: 65–95 years; mean $\pm$ SD = 80.1 $\pm$ 8.3 years), making it representative of older adult brain (Ridwan et al., 2021). Moreover, the construction approach of MIITRA was different from conventional template building, as it was constructed with state-of-the-art spatial normalization (Ridwan et al., 2021). LVV (46.95 mL) of the MIITRA template was closer to that of the aging population (Fig. 2), limiting the deformations needed to match the template.

A non-parametric approach was used to model tissue intensities, which was more suitable for CT images as aliasing effects responsible for poorly behaved intensity histograms are less pronounced than in MRI images (Ashburner et al., 2021). The used registration approach involved simultaneously minimizing two terms. One of these was a measure of similarity between the images, whereas the other was a measure of the roughness of the deformations. In the output, spatially normalized CT images were segmented, and deformation fields were generated. Then the combined deformation fields were applied to co-registered SPECT images, using B-spline interpolation based on a 4th° spline.

The default SPM12 spatial normalization pipeline used as the reference in the present study consists of applying the unified framework that alternates between classification (using ICBM152 TPMs) and registration. The same non-parametric approach used to model tissue intensities was applied in the default SPM12 approach.

2.3. Evaluation

Firstly, the performance of the spatial normalization was estimated using the comparison between the estimated LVV before warping and the LVV of the template, as well as between the estimated LVV after warping and the LVV of the template, as a robust spatial normalization should make the subject's LVV similar to that of the template. The volume difference was computed as follows: $VolumeDifference = \sqrt{|LVV_{template} - LVV_{CT}|}$ (5), where $LVV_{template}$ was the LVV of the template associated with the selected set of TPMs, and LVV_{CT} was the LVV of the spatially normalized CT image from one subject. The root was added to display values more clearly. The smaller was the *VolumeDifference* the better was the spatial normalization. The intersection between the polynomial fits of the differences between the LVV of the spatially normalized CT images and that of the template when performing both methods was used to identify the LVV cutoff from which the proposed method provides better performance.

Secondly, performance of the spatial normalization was estimated

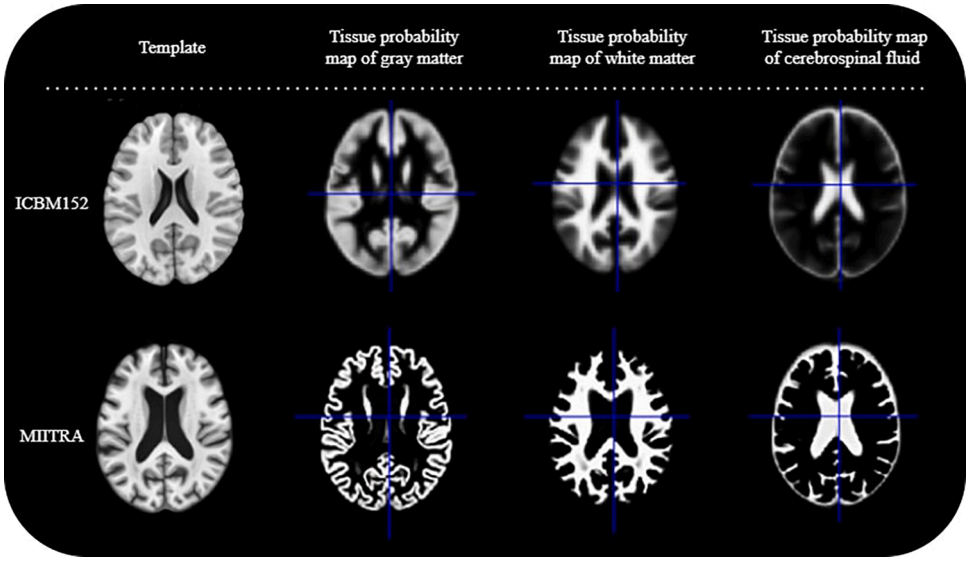

Fig. 2. Comparison between axial slices of SPM12 standard MRI template (top left) and MIITRA template (bottom left) as well as their respective tissue probability maps (TPMs). The voxel size of the standard TPMs is 1.5 × 1.5 × 1.5 mm^3; TPMs for MIITRA have a voxel size of 1 × 1 × 1 mm^3. The lateral ventricular volume (LVV) of MIITRA (46.95 mL) is greater than that of ICBM152 (29.38 mL). For TPMs, the brightest voxels indicate high probability of that tissue class.

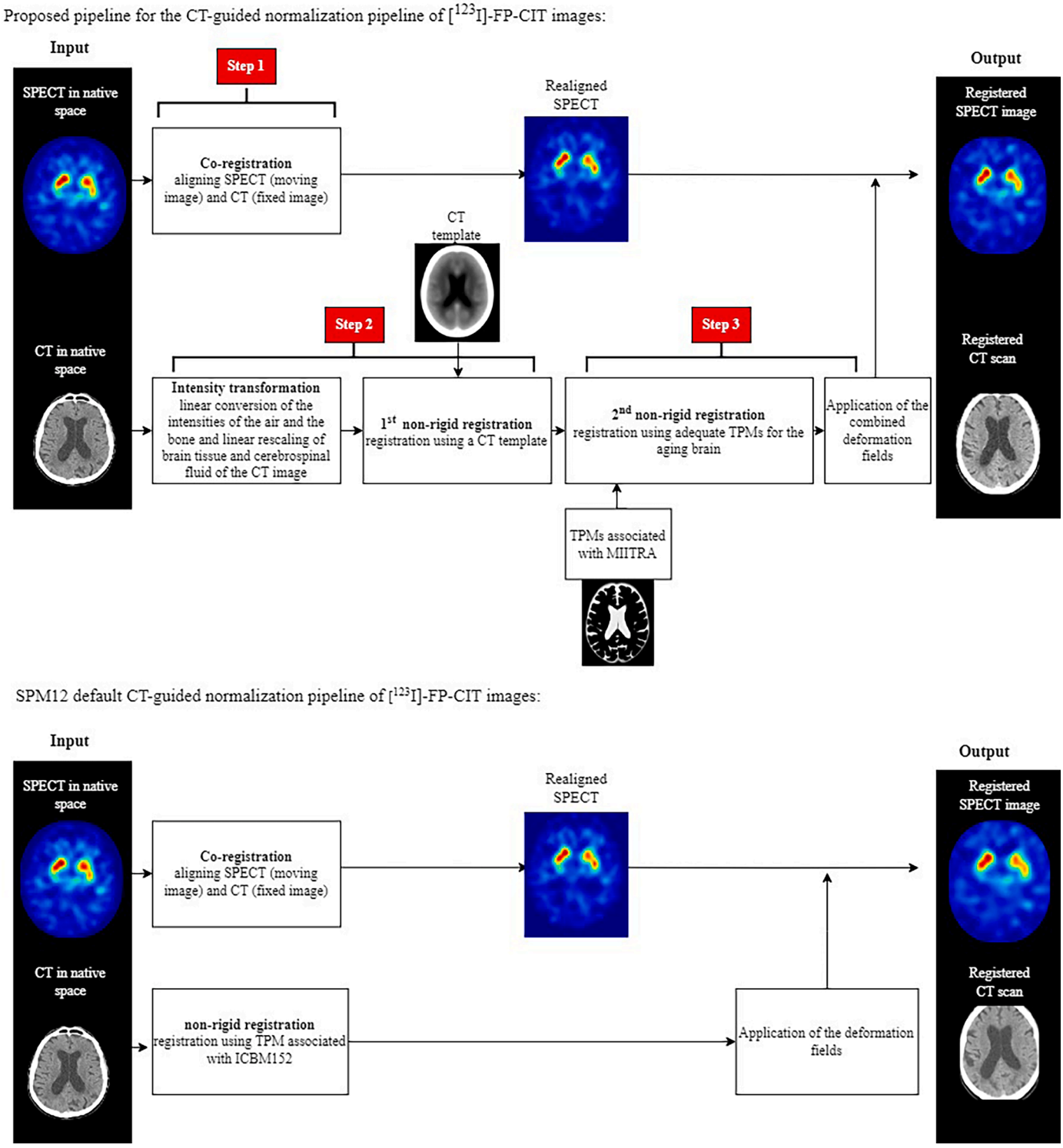

Fig. 3. Top: Pipeline of the proposed CT-guided spatial normalization of SPECT images. The CT image in the native space is spatially registered, and then the generated deformation fields are combined by the operation of "composition" and applied to the co-registered SPECT image. Bottom: SPM12 default CT-guided normalization.

using the overlap between the striatal VOIs (caudate and putamen) of the template and the spatially normalized lateral ventricles of subjects. Striatal VOIs were chosen, as their positioning is potentially impacted by the enlarged lateral ventricles. We measured the overlap between striatal VOIs generated from the template corresponding atlas and the lateral ventricles of the spatially normalized CT images as an indirect method to assess the correspondence between spatially normalized striatal regions of CT images and those of the used atlas, without the need of segmenting these anatomical regions on the CT image. This overlap was calculated as follows:

$$Overlap(\%) = 100.\frac{|LV \cap A_{VOIs}|}{|A_{VOIs}|} \quad (7)$$

Where LV were the lateral ventricles and A_{VOIs} were the striatal VOIs of

the atlas.

Additionally, we used the Dice score index (Shattuck et al., 2001; Fischmeister et al., 2013) to assess the performance of the segmentation of WM and GM, as it was jointly executed with the spatial normalization. Therefore, this was a complementary manner to assess the performance of the unified framework used both in SPM12 default spatial normalization and in the proposed pipeline. We calculated the Dice score index as follows:

$$\mathrm{Dice}(CT_{TPM},\ T_{TPM}) = 2.\frac{|CT_{TPM} \cap T_{TPM}|}{|CT_{TPM}| + |T_{TPM}|} \quad (6)$$

Where CT_{TPM} and T_{TPM} were the TPMs of WM and GM of the spatially normalized CT image and the MRI template respectively, normalized to template space and thresholded to 0.5. The notation $|.|$ represents the cardinality of these binary sets. The ground truth segmentation was considered as the MRI template's segmentation (T_{TPM}), as its own associated TPMs were used for tissue classification.

Lastly, we performed the semi-quantitative analysis of [^{123}I]-FP-CIT SPECT images using predefined striatal and occipital lobe VOIs. SBR was computed using the following formula (Innis et al., 2007):

$$SBR = (C_{voi} - C_{occipital}) / C_{occipital} \quad (8)$$

Where C_{voi} and $C_{occipital}$ are the mean uptakes of voxels within the caudate VOI, putamen VOI and within the occipital lobe, respectively. The reference was the occipital region as it has negligible density of tracer-binding sites.

As the spatial normalization influences the accuracy of the VOI positioning (Gispert et al., 2003), it is expected that in our visually normal cohort of [^{123}I]-FP-CIT SPECT images, poorly positioned VOIs reduce the value of SBRs. Since there was no labelled atlas corresponding to the MIITRA template available at the time of the study, new striatal VOIs were created. These VOIs were a manually modified version of ICBM152 corresponding atlas's VOIs, as we overlaid these VOIs to better match the MIITRA template. It is worth noting that the volume of the striatal VOIs were fixed and did not take into consideration potential volumetric decrease due to aging (Coupé et al., 2019).

2.4. Statistical analyses

Descriptive statistics are presented as follows: continuous variables as means and SD or median and interquartile range (IQR) and compared using the Wilcoxon test or the Student's *t*-test, according to their distribution. The linear regression analyses were performed to estimate the relationship of the LVV after the spatial normalization and caudate SBR with the tested independent variable: initial LVV. The linear regression line was defined as y = slope (± Standard Error [SE]) × initial LVV + intercept (± SE). The relationship between *VolumeDifference* and the independent variable: initial LVV was analyzed using polynomial regression. The interaction between age and LVV and their impact on the caudate SBR were tested using the following linear model: SBR ~ age + LVV + age:LVV (the product of age and LVV). All statistical analyses were performed using MATLAB (R2021a; The MathWorks Inc., Natick, MA, USA).

3. Results

3.1. LVV distribution and correlation with age

After assessing LVV through the two segmentation techniques, and conducting visual inspection, 6 subjects were excluded for failed CSF segmentation (2.5 %). In total 231 subjects (mean age ± SD = 61.9 ± 15.5 years) were included in the statistical analysis. LVV ranged from 12 to 109 mL (Fig. 4), and the mean LVV ± SD was 48.58 ± 21.96 mL. Age and the LVV were moderately correlated (r = 0.65). Age was also moderately correlated with LVV of the left and the right hemispheres (*r*

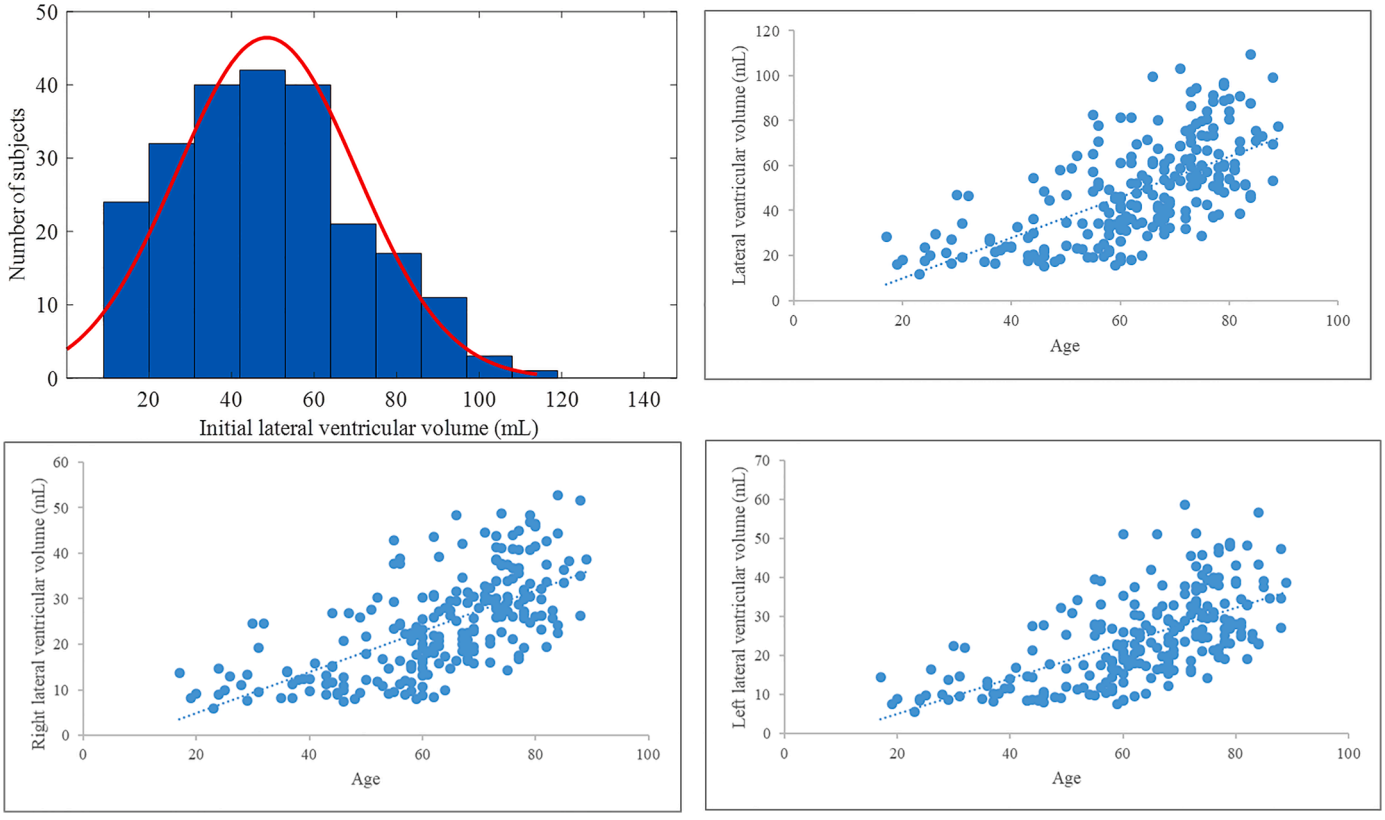

Fig. 4. Lateral ventricular volumes (LVV) distribution and the fitted normal distribution (red continuous line) are displayed in the top left graph. Total LVV (top right graph), the left LVV (bottom left) and the right LVV (bottom right) are displayed according to age (years).

= 0.62 and $r = 0.64$, respectively) highlighting age-related enlargement of the lateral ventricles.

3.2. LVV after spatial normalization

The intersection between the polynomial fits of *VolumeDifference* after performing both SPM12 default spatial normalization and the proposed pipeline indicated that above 30 mL, LVVs of subjects were closer to the template's LVV after performing the proposed pipeline (mean *VolumeDifference* = 1.92 for the proposed pipeline and mean *VolumeDifference* = 4.48 for SPM12 default spatial normalization). Below 30 mL (corresponding to approximately 42 years of age), using SPM12 default normalization provided slightly better results (mean *VolumeDifference* = 1.33) than the proposed pipeline (mean *VolumeDifference* = 2.15; Fig. 5).

The comparison between LVV after SPM12 default spatial normalization (linear regression: y = 0.7156 (± 0.0095) × x + 10.97 (± 0.5073), R^2 = 0.96) and those after the proposed pipeline (linear regression: $y = 0.2371$ (± 0.0058) × x + 44.427 (± 0.3125), $R^2 = 0.94$), confirmed that spatial normalization accuracy was improved significantly ($P < 0.001$). After application of the proposed pipeline, LVVs were much closer to that of the template (the intercept value was closer to the LVV of the template and the slope was closer to zero; Fig. 6). Moreover, the SD of LVV decreased from 16.13 mL to 6.62 mL.

3.3. Overlap of the template' striatal VOIs with lateral ventricles of the spatially normalized CT images

For the sake of simplicity, we will refer to the VOIs from atlases corresponding to the used templates as template's VOIs. Fig. 7 presents an example of the superposition of the template's caudate VOI on a SPECT/CT image (LVV = 69.62 mL) using the SPM12 default spatial normalization and the proposed spatial normalization; the overlap of the template's caudate VOI with subjects' lateral ventricles was 55.86 % of the VOI using the former and 11.31 % using the proposed spatial normalization pipeline.

When using the SPM12 default spatial normalization, the mean ± SD overlap between the template's caudate VOI and the lateral ventricles represented 38.40 % ± 19.48 % of the VOI (Fig. 8). For subjects with an LVV above the median LVV, this increased to 54.11 % ± 13.37 % ($P < 0.001$). However, using the proposed pipeline with MIITRA TPMs, the mean overlap was equal to 9.13 % (± 1.41 %, $P < 0.001$) of the initial volume of the template's caudate VOI. While for subjects with an LVV above the median LVV, the mean overlap was 9.79 % (± 1.39 %, $P < 0.001$).

The overlap between putamen VOI and the lateral ventricles was negligible (<0.001 % of the putamen VOI) for both methods. In other words, evaluating striatal VOIs overlap with the lateral ventricles amounted only to evaluate caudate VOI overlap with the lateral ventricles.

3.4. Dice score index

After performing the default spatial normalization within SPM12, the median Dice score index was 0.59 (IQR, 0.58–0.60) for the combined GM and WM. The median score was greater (0.64, $P < 0.001$, IQR, 0.62–0.66) with the new pipeline (Fig. 9).

3.5. Impact on specific binding ratios

The mean ± SD and SBR values for the caudate were 1.77 ± 0.79 using the default spatial normalization within SPM12, and this was significantly greater when using the proposed approach (mean caudate SBR ± SD = 2.38 ± 0.51, $P < 0.0001$; Fig. 10). The mean putamen SBR value obtained after the proposed spatial normalization (2.75 ± 0.54) were not significantly different to that obtained using default SPM12 spatial normalization (2.83 ± 0.52, $P > 0.05$; Fig. 11).

The relationship between SBR of caudate and LVV was analyzed using linear regression (Fig. 12); the R^2 for proposed pipeline (0.22) was lower than that of the default SPM12 spatial normalization (0.53) indicating a lower impact of LVV on SBR values (Table 2)

Additionally, the relationship between caudate SBR, age and LVV

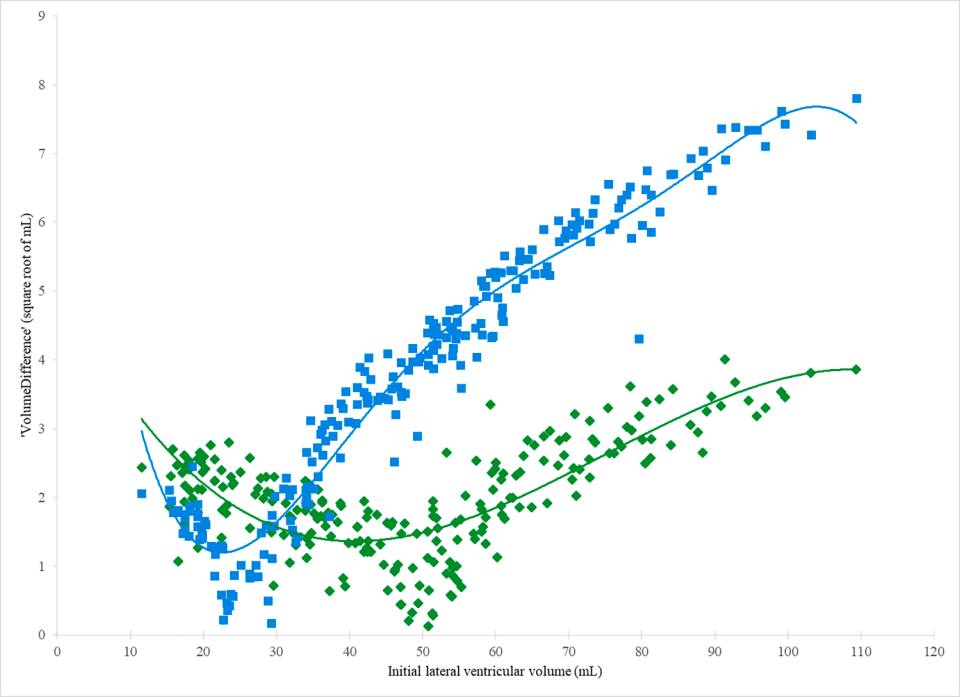

Fig. 5. Scatter plot and polynomial fits of the difference between lateral ventricular volume (LVV) of each spatially normalized CT image and that of the template after using SPM12 default spatial normalization (light blue) and after the proposed pipeline (green). Volume differences closer to zero suggest a more accurate spatial normalization.

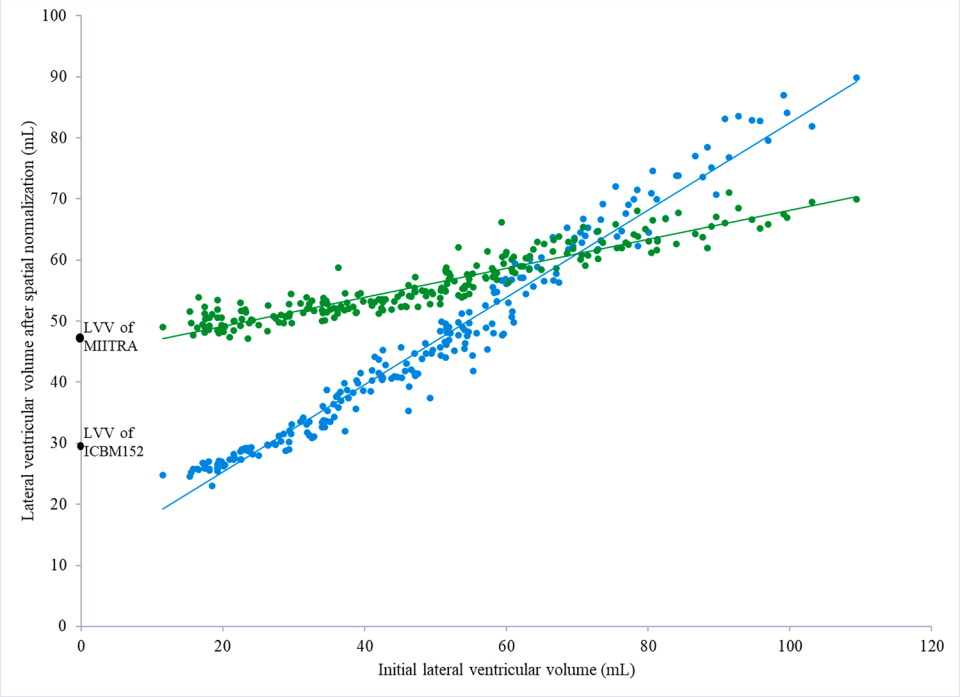

Fig. 6. Comparison of lateral ventricular volumes (LVV) after SPM12 spatial normalization (light blue dots) vs after the proposed spatial normalization (green dots), according to the initial lateral ventricular volume. A linear fit intercept equaling the LVV of the used template and a slope equaling zero means a perfect spatial normalization, as the lateral ventricles of the spatially normalized CT images match precisely those of the template.

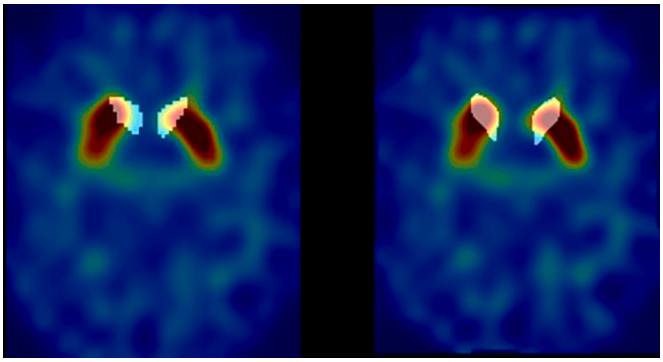

Fig. 7. Comparison between the superposition of the template's caudate volume of interest (VOI; white) on a SPECT image, in case of SPM12 default spatial normalization (left) and the proposed spatial normalization (right). After performing the proposed spatial normalization, the overlap between the caudate VOI and the anatomical caudate was enhanced, and a larger area of caudate uptake was measured.

was analyzed using regression analysis. According to the coefficient estimates for each corresponding term in the model: SBR ~ age + LVV + age:LVV ($R^2 = 0.621$ for the SPM12 default CT-guided spatial normalization and $R^2 = 0.38$ for the proposed pipeline), age and LVV were significant predictors for both pipelines ($P < 0.05$). The coefficient of the interaction term is statistically significant ($P < 0.05$) for both methods as well. However, the proposed pipeline reduced the significance of the correlation between caudate SBR and the interaction between age and LVV (from $P = 0.02$ to $P = 0.04$).

4. Discussion

In the present study, the proposed CT-guided pipeline increased the performance of warping older brains to a standard stereotaxic space as compared to the default SPM12 CT-guided pipeline. The improved normalization to a standard space decreased the overlap between the spatially normalized lateral ventricles and the caudate VOI. In the cohort of visually normal [^{123}I]-FP-CIT scan, caudate SBR increased by reducing its underestimation due to lateral ventricular enlargement and VOI misalignment.

The proposed pipeline does not require an MRI to be readily used with SPECT or PET CT hybrid scanner even though MRI-guided spatial normalization remains the gold standard. Presotto et al. (2018) reported that CT- and MRI-based normalized GM maps overlapped within 1 mm in 90 % of voxels (isotropic voxel size of 1 mm), validating the feasibility of a CT-based pipeline for PET spatial normalization. Kim et al. (2015) also confirmed that the CT-guided spatial normalization had comparable capability to the MRI-guided method for the analysis of [^{18}F]-FP-CIT PET. In addition, it has also been reported that low dose CT can substitute MRI-guided spatial normalization (Matsuda et al., 2021). However, these studies did not include the impact of enlarged lateral ventricles on the performance of spatial normalization.

The proposed spatial normalization pipeline was specifically developed for the spatial normalization of CT scans. In the 1st step we applied an intensity transformation rather than an explicit skull stripping, which may be prone to errors and is time consuming. Intensity transformation increases the intensity range representing the CSF and brain tissue, and reduces intensity contrast between the skull and brain tissue. Kim et al. (2015) reported that there was no large difference between the performance of spatial normalization using a skull-stripped CT-guided method and an intensity-transformed CT-guided method. The 1st non-rigid registration with the CT template was intended to ease the functioning of the non-rigid registration with TPMs as its LVV was closer to the median LVV of the included subjects. Therefore, the aim of this step was to correct partially gross spatial variability of CT brain images and permit a more accurate non-linear spatial registration when using TPMs. In the 2nd non-rigid registration, we used TPMs to conduct spatial normalization. MRI TPMs are generally used for both CT and MRI-guided spatial normalization (Presotto et al., 2018). TPMs from the MIITRA improved, as expected, the spatial normalization for cases with LVV greater than 30 mL. We also tested an additional approach for the

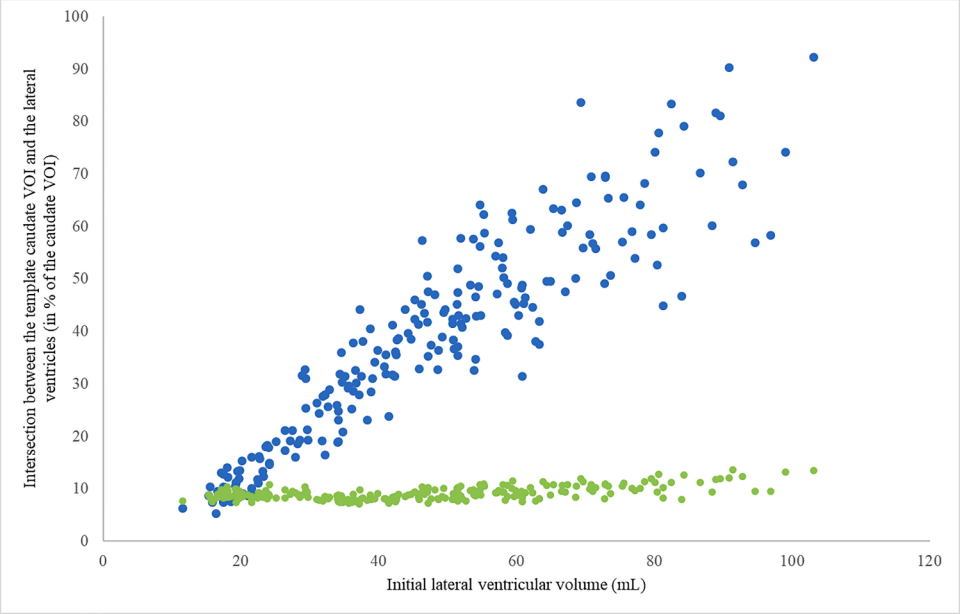

Fig. 8. Comparison of the overlap between the template's caudate volume of interest (VOI) and the lateral ventricles of subjects after SPM12 default spatial normalization (blue dots) vs after the proposed spatial normalization pipeline (green dots), as % of the VOI volume. A more robust spatial normalization means less overlap ($y = 0$ when the spatial normalization is perfect).

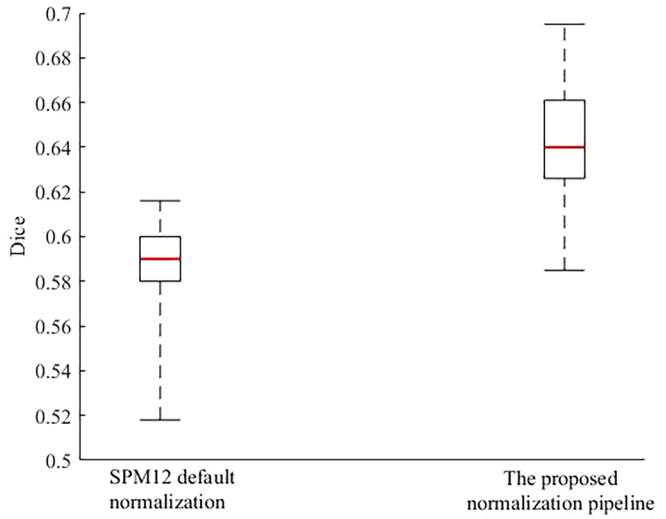

Fig. 9. Box plot of Dice values using SPM12 default spatial normalization vs the proposed spatial normalization approach for the combined gray matter and white matter (GM+WM). The central red mark indicates the median, and the bottom and top edges of the box indicate the 25th and 75th percentiles, respectively. The whiskers stand for the minimum and the maximum value of the data set.

2nd step of the proposed pipeline in which the set of TPMs was chosen according to the estimated LVV (not reported herein). In this approach, SPM12 TPMs were used when LVV were below a certain cutoff instead of using MIITRA TPMs in all cases. Standard TPMs found in SPM12 provided accurate spatial normalization results when the LVV was lower than that of the ICBM152. Below an LVV of 30 mL (LVV of ICBM152 = 29.38 mL), using SPM12 default spatial normalization resulted in a mean volumetric difference of 1.77 mL between the spatially normalized lateral ventricles and the lateral ventricles of the template. However, switching TPMs provided moderate enhancement of the spatial normalization as compared to the proposed single-template approach. The large proportion of elderly patients in the study cohort, who had large ventricles, made this refinement unnecessary. However, we underline that the set of TPMs should be adapted to the studied population. This is in line with the study reported by Brudfors et al. (2020) in which it was found that a registration to an optimal space can increase the accuracy of spatial normalization instead of a coarse registration to MNI space. The combination of all these steps improved the process of segmenting images into different classes using a mixture model algorithm. This resulted in a greater Dice score index (for the combined segmentation of WM and GM), and in a closer CT LVV (for segmented CSF) to that of the template after the spatial normalization, providing higher spatial normalization accuracy compared to the reference method.

Reig et al. (2007) focused on the impact of PET spatial normalization in pathologic brain using a PET template in the measurement of PET metabolic activity. The mean overlap between the spatially normalized caudate and the caudate of the template was lower than 50 %. This caused miscalculation for quantitative analysis relying on the caudate VOI. The authors reported a significant correlation between the size of the lateral ventricles and underestimation of metabolic activity of the caudate and warned against this source of error that should be taken into account. Likewise, in the present study the reduced amount of overlap between the spatially normalized lateral ventricles and the caudate VOI was highly correlated with the increase of caudate SBR values when performing the proposed pipeline as compared to the default pipeline. No overlap was noted between the normalized lateral ventricles and the putamen VOI from the standard space using both pipelines. Even though the putamen is considered as the most relevant brain region in [^{123}I]-FP-CIT studies for idiopathic Parkinson's disease, a correct measure of the uptake in the caudate allows assessing striatum uptake, which, combined with quantitative parameters such as putamen-to-caudate ratios and asymmetry index, can be useful in cases where a clear evaluation cannot be made. These quantitative parameters are more independent from the reconstruction algorithm and background activity making them relevant data (Koch et al., 2005). In addition, subregional patterns, including caudate uptake, can be used to suggest atypical parkinsonian syndrome as suggested in the last EANM guidelines reported by Morbelli et al. (2020). Even though they often overlap with Parkinson's disease features; for example, in progressive supranuclear palsy, uptake reduction tends to be more symmetric and to involve the caudate nucleus earlier in disease course as compared with

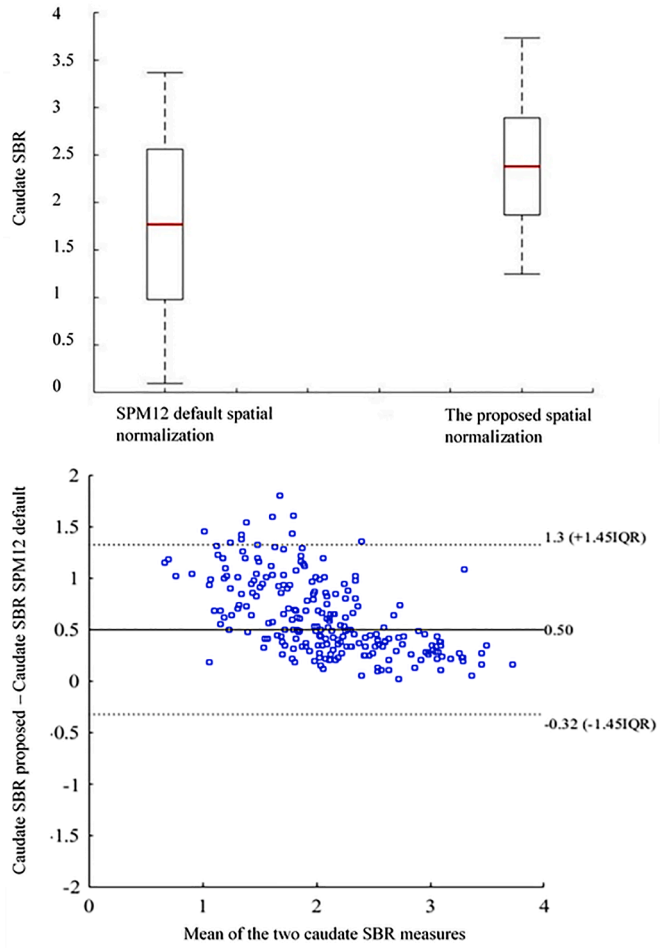

Fig. 10. Top: Plot of caudate specific binding ratio (SBR) values using SPM12 default spatial normalization vs the proposed spatial normalization pipeline. The central red mark indicates the mean, the box represents the standard deviation (SD), and the whiskers stand for the minimum and the maximum value of the data set. Bottom: Bland-Altman plot with limits of agreement indicating ±1.451*IQR (dotted lines).

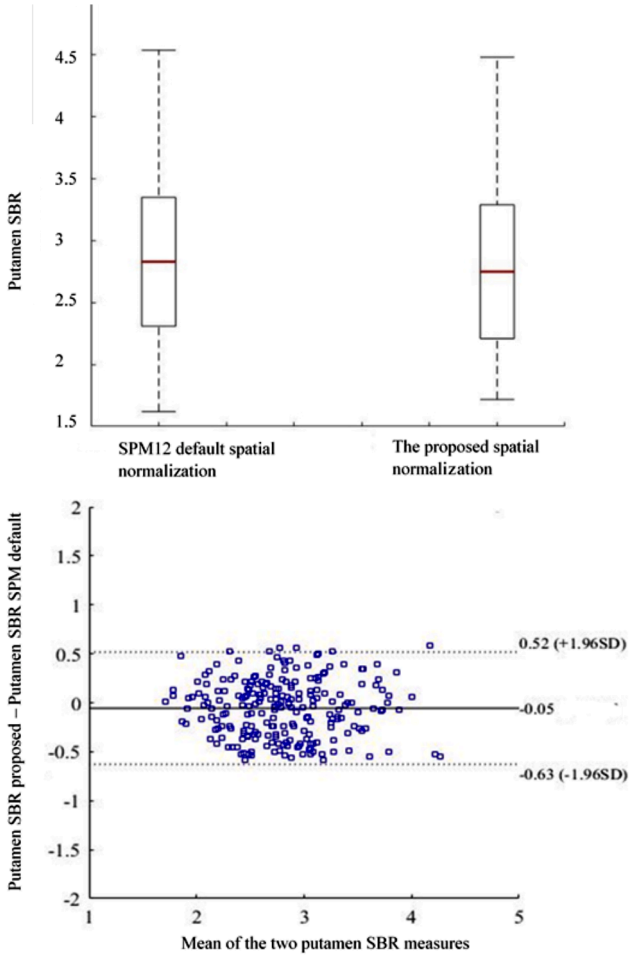

Fig. 11. Top: Plot of putamen specific binding ratio (SBR) values using SPM12 default spatial normalization vs the proposed spatial normalization pipeline. The central red mark indicates the mean, the box represents the standard deviation (SD), and the whiskers stand for the minimum and the maximum value of the data set. Bottom: Bland-Altman plot with limits of agreement indicating ±1.96*SD (dotted lines).

idiopathic Parkinson disease. Furthermore, the measurement of the caudate function is relevant as functional implications of the caudate have been recorded in Parkinson's disease (Pasquini et al., 2019), Alzheimer's disease (Xiong et al., 2022), Huntington's disease (Agus et al., 2019), and schizophrenia (Kirino et al., 2019) in which lateral ventricular enlargement may also occur.

As we evaluate the anatomical reliability of automated brain tissue classification through LVV, we had to accurately estimate it. Accurate LVV quantification is also important in studies investigating cortical atrophy and age-related brain changes, such as neurodegenerative diseases (Yepes-Calderon and McComb 2022). While there was no large dataset-derived standard established for normal or pathological LVV, Maragkos et al. (2021) used a deep learning-based segmentation to conduct LVV measurements in more than 13,851 patients; scans classified as "normal" had a median LVV of 15.7 mL (IQR, 11.1–22.2) and those classified as "hydrocephalus" had a median LVV of 82.1 mL (IQR, 51.1–126.0); those classified as "atrophy" had a median LVV that was approximately comparable to that found in the present study (47.11 mL) which is concordant as the studied cohort contained mainly older adults (mean age > 60 years) with brain structural changes such as atrophy.

The present study has some limitations. First of all, we did not take into account the partial volume effect (PVE). Indeed, due to PVE, biases can be introduced when tracer uptake in small VOI is measured. PVE is the 3-dimensional image blurring secondary to the finite spatial

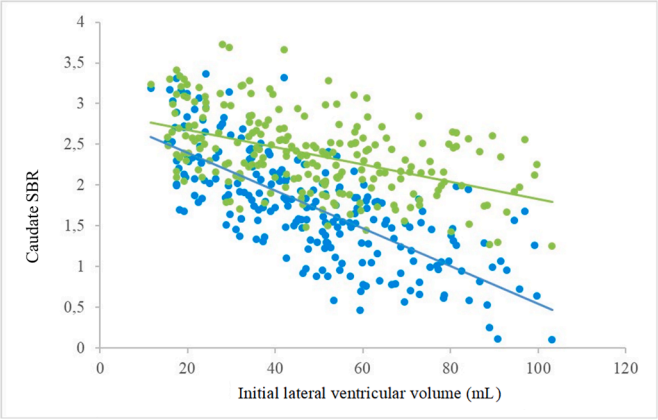

Fig. 12. Caudate specific binding ratio (SBR) values according to the lateral ventricular volume (LVV) with SPM12 default spatial normalization (light blue dots) vs with the proposed spatial normalization (green dots), and their respective linear fits.

Table 2
Linear regression analysis of caudate uptake, using SPM12 default spatial normalization vs the proposed spatial normalization pipeline.

	SPM12 default spatial normalization module Values for the caudate	The proposed spatial normalization pipeline
Mean SBR ± SD	1.77 ± 0.79	2.38 ± 0.51
y = slope (± SE) × initial LVV + intercept (±SE)	Y = - 0.027 (± 0.0014) × LVV + 2.86 (±0.0744)	Y = - 0.011 (± 0.0013) × LVV + 2.89 (±0.0691)
P value	<0.001	<0.001
R^2	0.53	0.22

resolution of the SPECT system which causes spillover between regions and may reduce maximum measured activity. For example, to compensate these effects, multiplicative recovery coefficients have been applied in several studies (Gnesin et al., 2016; Peters et al., 2019). However, these recovery coefficients always require some type of calibration either by experiments or simulation and are mostly measured based on spherical objects in phantoms while being size-dependent and reconstruction-algorithm-dependent (Ismail and Mansor, 2019). Expanded VOIs can also be used to include both the object region and the spill-out region so that all of the spill-out uptakes are captured (Bian et al., 2023). This accuracy of this method depends on how well the VOI can be delineated. For irregular-shaped small regions such the caudate and the putamen, the delineation can be challenging. In the present study, we focused on the recovery of the "lost" striatal uptake that was not captured due to lateral ventricular enlargement and VOI mispositioning rather than obtaining "true" uptake value thanks to a partial volume correction. Indeed, no ground-truth for SBR computation was available (e.g., using manually derived individual specific VOI or phantom acquisition) to assess the "true" uptake value. Additionally, expansion of the striatal VOIs, a potential PVE correction method, could have hampered the evaluation of the spatial normalization accuracy by potentially compensating the impact of lateral ventricles enlargement.

Second, the influence of CT image quality and image reconstruction on the performance and robustness of the spatial normalization pipeline was not studied. However, several studies suggest the feasibility of low-dose CT guided spatial normalization of PET images (Kim et al., 2015; Presotto et al., 2018; Matsuda et al., 2021). Nevertheless, future studies are needed to assess whether the use of low dose CT provides the same improvements when performing the proposed approach and validate the pipeline using data from multiple sites with different acquisition and reconstruction protocols.

Third, hybrid nuclear medicine scanners use hardware calibration to align SPECT and CT images; however, accidental misalignment may occur (head movement between the two acquisitions). The added rigid registration step was intended to prevent any potential shift between the two modalities. However, it is worth noting that caution should be taken when performing rigid registration (for both SPECT/CT and PET/CT), mainly when the imaging with various radio ligands of which binding is limited to some regions of the brain or of which binding pattern is quite different between the controls and subjects.

Fourth, the volume of the caudate VOI was fixed and did not take into consideration potential structural changes due to aging (Bauer et al., 2015), which may affect the overlay of the VOIs. Fifthly, manually labelled brain regions could have been used as a gold standard, offering a more reliable measure of spatial normalization accuracy (Klein et al., 2009), however this approach could not be adopted in the present study as manual labelling is time consuming and cannot be performed in case of larger datasets.

5. Conclusion

The automatic CT-guided spatial normalization used herein led to a less biased spatial normalization of SPECT images, resulting in an improved quantitative analysis. The proposed pipeline could be implemented in clinical routine to perform a more robust SBR computation using hybrid imaging.

Statements and declarations

Information sharing statement

The datasets generated and/or analyzed during the current study are not publicly available due institutional restrictions on patient confidentiality, prior consent, and privacy.

Compliance with ethical standards

We certify that the study was performed in accordance with the ethical standards as laid down in the 1964 Declaration of Helsinki and its later amendments or comparable ethical standards.

This research project retrospectively included data acquired in clinical settings after obtaining written informed consent from the patient for publication of the present study and accompanying images (MR-004 French research type). The institutional medical ethics committee of the Hospices Civils de Lyon approved the protocol on October 14, 2021, under the following reference: 21_5593.

Funding

The present study did not receive any specific grant from funding agencies in the public, commercial, or not-for-profit sectors.

Data and code availability statement

The datasets generated and/or analyzed during the current study are not publicly available due institutional restrictions on patient confidentiality, prior consent, and privacy.

CRediT authorship contribution statement

Alae Eddine El Barkaoui: Conceptualization, Methodology, Software, Validation, Formal analysis, Data curation, Writing – original draft, Writing – review & editing, Visualization. **Christian Scheiber:** Conceptualization, Methodology, Software, Validation, Formal analysis, Data curation, Writing – original draft, Writing – review & editing, Visualization, Supervision. **Thomas Grenier:** Conceptualization, Methodology, Formal analysis, Writing – review & editing, Visualization. **Marc Janier:** Writing – review & editing, Project administration. **Anthime Flaus:** Conceptualization, Methodology, Writing – review & editing.

Declaration of competing interest

The authors have no financial or non-financial interests to disclose.

Acknowledgments

We would like to thank all the technologists, technical staff and clinical research assistants at the Nuclear Medicine Department of Hospices Civils de Lyon (Lyon, France). The authors thank Perrine Tylski for help in CT dosimetry. The authors thank also Philip Robinson (Hospices Civils de Lyon) for help in manuscript preparation.

References

Agus, F., Crespo, D., Myers, R.H., Labadorf, A., 2019. The caudate nucleus undergoes dramatic and unique transcriptional changes in human prodromal Huntington's disease brain. BMC Med. Genom. 12 (1), 137. https://doi.org/10.1186/s12920-019-0581-9.

Allen, J.S., Bruss, J., Mehta, S., Grabowski, T., Brown, C.K., Damasio, H., 2008. Effects of spatial transformation on regional brain volume estimates. Neuroimage 42 (2), 535–547. https://doi.org/10.1016/j.neuroimage.2008.05.047.

Ashburner, J., Friston, K.J., 2005. Unified segmentation. Neuroimage 26 (3), 839–851. https://doi.org/10.1016/j.neuroimage.2005.02.018.

Ashburner J., Barnes G., Chen C.-C., Daunizeau J., Flandin G., Friston K., et al. (2021). SPM 12 Manual. Available at: http://www.fil.ion.ucl.ac.uk/spm/doc/spm12_manual.pdf.

Bauer, E., Toepper, M., Gebhardt, H., Gallhofer, B., Sammer, G., 2015. The significance of caudate volume for age-related associative memory decline. Brain Res. 1622, 137–148. https://doi.org/10.1016/j.brainres.2015.06.026.

Bian, J., James, J.R., Wagner, R., Halama, J., 2023. Quantify total activity by volume-of-interest expansion with clinical SPECT/CT systems, a phantom study. J. Appl. Clin. Med. Phys. 24 (1), e13828. https://doi.org/10.1002/acm2.13828.

Brett, M., Johnsrude, I.S., Owen, A.M., 2002. The problem of functional localization in the human brain. Nat. Rev. Neurosci. 3 (3), 243–249. https://doi.org/10.1038/nrn756.

Brudfors, M., Balbastre, Y., Flandin, G., Nachev, P., & Ashburner, J. (2020). Flexible Bayesian Modelling for Nonlinear Image Registration (Vol. 12263, pp. 253–263). doi:10.1007/978-3-030-59716-0_25.

Carmichael, O.T., Kuller, L.H., Lopez, O.L., Thompson, P.M., Dutton, R.A., Lu, A., et al., 2007. Ventricular volume and dementia progression in the cardiovascular Health Study. Neurobiol. Aging 28 (3), 389–397. https://doi.org/10.1016/j.neurobiolaging.2006.01.006.

Colloby, S.J., Firbank, M.J., Vasudev, A., Parry, S.W., Thomas, A.J., O'Brien, J.T, 2011. Cortical thickness and VBM-DARTEL in late-life depression. J. Affect. Disord. 133 (1–2), 158–164. https://doi.org/10.1016/j.jad.2011.04.010.

Coupé, P., Manjón, J.V., Lanuza, E., Catheline, G., 2019. Lifespan changes of the human brain in Alzheimer's disease. Sci. Rep. 9 (1), 3998. https://doi.org/10.1038/s41598-019-39809-8.

Dalca, A., Rakic, M., Guttag, J., Sabuncu, M., 2019. Learning Conditional Deformable Templates with Convolutional Networks. Adv. Neural. Inf. Process. Syst. 32 https://doi.org/10.48550/arXiv.1908.02738.

Della Rosa, P.A., Cerami, C., Gallivanone, F., Prestia, A., Caroli, A., Castiglioni, I., et al., 2014. A standardized [18F]-FDG-PET template for spatial normalization in statistical parametric mapping of dementia. Neuroinformatics 12 (4), 575–593. https://doi.org/10.1007/s12021-014-9235-4.

Eloyan, A., Shou, H., Shinohara, R.T., Sweeney, E.M., Nebel, M.B., Cuzzocreo, J.L., et al., 2014. Health effects of lesion localization in multiple sclerosis: spatial registration and confounding adjustment. PLoS One 9 (9), e107263. https://doi.org/10.1371/journal.pone.0107263.

Fahmi, R., Platsch, G., Sadr, A.B., Gouttard, S., Thobois, S., Zuehlsdorff, S., Scheiber, C., 2020. Single-site 123I-FP-CIT reference values from individuals with non-degenerative parkinsonism—comparison with values from healthy volunteers. Eur. J. Hybrid Imaging 4 (1), 5. https://doi.org/10.1186/s41824-020-0074-2.

Fischl, B., Salat, D.H., van der Kouwe, A.J.W., Makris, N., Ségonne, F., Quinn, B.T., Dale, A.M., 2004. Sequence-independent segmentation of magnetic resonance images. Neuroimage 23, S69–S84. https://doi.org/10.1016/j.neuroimage.2004.07.016.

Fischmeister, F.P.S., Höllinger, I., Klinger, N., Geissler, A., Wurnig, M.C., Matt, E., et al., 2013. The benefits of skull stripping in the normalization of clinical fMRI data. NeuroImage Clin. 3, 369–380. https://doi.org/10.1016/j.nicl.2013.09.007.

Ganzetti, M., Liu, Q., Mantini, D., 2018. A spatial registration toolbox for structural MR imaging of the aging brain. Neuroinformatics 16. https://doi.org/10.1007/s12021-018-9355-3.

Gispert, J.D., Pascau, J., Reig, S., Martínez-Lázaro, R., Molina, V., García-Barreno, P., Desco, M., 2003. Influence of the normalization template on the outcome of statistical parametric mapping of PET scans. Neuroimage 19 (3), 601–612. https://doi.org/10.1016/S1053-8119(03)00072-7.

Gnesin, S., Leite Ferreira, P., Malterre, J., Laub, P., Prior, J.O., Verdun, F.R., 2016. Phantom validation of Tc-99m absolute quantification in a SPECT/CT commercial device. Comput. Math. Methods Med., 4360371 https://doi.org/10.1155/2016/4360371, 2016.

Innis, R.B., Cunningham, V.J., Delforge, J., Fujita, M., Gjedde, A., Gunn, R.N., et al., 2007. Consensus nomenclature for *in vivo* imaging of reversibly binding radioligands. J. Cereb. Blood Flow Metab. 27 (9), 1533–1539. https://doi.org/10.1038/sj.jcbfm.9600493.

Ismail, F.S., Mansor, S., 2019. Impact of resolution recovery in quantitative 99mTc SPECT/CT cardiac phantom studies. J. Med. Imaging Radiat. Sci. 50 (3), 449–453. https://doi.org/10.1016/j.jmir.2019.05.007.

Izquierdo-Garcia, D., Hansen, A.E., Förster, S., Benoit, D., Schachoff, S., Fürst, S., et al., 2014. An SPM8-based approach for attenuation correction combining segmentation and non-rigid template formation: application to simultaneous PET/MR brain imaging. J. Nucl. Med. 55 (11), 1825–1830. https://doi.org/10.2967/jnumed.113.136341.

Kempton, M.J., Underwood, T.S.A., Brunton, S., Stylios, F., Schmechtig, A., Ettinger, U., et al., 2011. A comprehensive testing protocol for MRI neuroanatomical segmentation techniques: evaluation of a novel lateral ventricle segmentation method. Neuroimage 58 (4), 1051–1059. https://doi.org/10.1016/j.neuroimage.2011.06.080.

Kennedy, K.M., Erickson, K.I., Rodrigue, K.M., Voss, M.W., Colcombe, S.J., Kramer, A.F., et al., 2009. Age-related differences in regional brain volumes: a comparison of optimized voxel-based morphometry to manual volumetry. Neurobiol. Aging 30 (10), 1657–1676. https://doi.org/10.1016/j.neurobiolaging.2007.12.020.

Kim, J.S., Cho, H., Choi, J.Y., Lee, S.H., Ryu, Y.H., Lyoo, C.H., Lee, M.S., 2015. Feasibility of computed tomography-guided methods for spatial normalization of dopamine transporter positron emission tomography image. PLoS One 10 (7), e0132585. https://doi.org/10.1371/journal.pone.0132585.

Kirino, E., Tanaka, S., Fukuta, M., Inami, R., Inoue, R., Aoki, S., 2019. Functional connectivity of the caudate in schizophrenia evaluated with simultaneous resting-state functional MRI and electroencephalography recordings. Neuropsychobiology 77 (4), 165–175. https://doi.org/10.1159/000490429.

Klein, A., Andersson, J., Ardekani, B.A., Ashburner, J., Avants, B., Chiang, M.C., et al., 2009. Evaluation of 14 nonlinear deformation algorithms applied to human brain MRI registration. Neuroimage 46 (3), 786–802. https://doi.org/10.1016/j.neuroimage.2008.12.037.

Koch, W., Hamann, C., Welsch, J., Pöpperl, G., Radau, P.E., Tatsch, K., 2005. Is iterative reconstruction an alternative to filtered backprojection in routine processing of dopamine transporter SPECT studies? J. Nucl. Med. 46 (11), 1804–1811.

Krebs, J., Delingette, H., Mailhe, B., Ayache, N., Mansi, T., 2019. Learning a probabilistic model for diffeomorphic registration. IEEE Trans. Med. Imaging. https://doi.org/10.1109/TMI.2019.2897112. PP, 1–1.

Lorio, S., Fresard, S., Adaszewski, S., Kherif, F., Chowdhury, R., Frackowiak, R.S., et al., 2016. New tissue priors for improved automated classification of subcortical brain structures on MRI. Neuroimage 130, 157–166. https://doi.org/10.1016/j.neuroimage.2016.01.062.

Makowski, C., Béland, S., Kostopoulos, P., Bhagwat, N., Devenyi, G.A., Malla, A.K., et al., 2018. Evaluating accuracy of striatal, pallidal, and thalamic segmentation methods: comparing automated approaches to manual delineation. Neuroimage 170, 182–198. https://doi.org/10.1016/j.neuroimage.2017.02.069.

Maragkos, G.A., Filippidis, A.S., Chilamkurthy, S., Salem, M.M., Tanamala, S., Gomez-Paz, S., et al., 2021. Automated lateral ventricular and cranial vault volume measurements in 13,851 patients using deep learning algorithms. World Neurosurg. 148, e363–e373. https://doi.org/10.1016/j.wneu.2020.12.148.

Martino, M.E., de Villoria, J.G., Lacalle-Aurioles, M., Olazarán, J., Cruz, I., Navarro, E., et al., 2013. Comparison of different methods of spatial normalization of FDG-PET brain images in the voxel-wise analysis of MCI patients and controls. Ann. Nucl. Med. 27 (7), 600–609. https://doi.org/10.1007/s12149-013-0723-7.

Matsuda, H., Yamao, T., Shakado, M., Shigemoto, Y., Okita, K., Sato, N., 2021. Amyloid PET quantification using low-dose CT-guided anatomic standardization. EJNMMI Res. 11 (1), 125. https://doi.org/10.1186/s13550-021-00867-7.

Morbelli, S., Esposito, G., Arbizu, J., Barthel, H., Boellaard, R., Bohnen, N.I., et al., 2020. EANM practice guideline/SNMMI procedure standard for dopaminergic imaging in Parkinsonian syndromes 1.0. Eur. J. Nucl. Med. Mol. ImAging 47 (8), 1885–1912. https://doi.org/10.1007/s00259-020-04817-8.

Niaz, M.R., Ridwan, A.R., Wu, Y., , Alzheimer's Disease Neuroimaging Initiative, Bennett, D.A., Arfanakis, K., 2022. Development and evaluation of a high resolution 0.5mm isotropic T1-weighted template of the older adult brain. Neuroimage 248, 118869. https://doi.org/10.1016/j.neuroimage.2021.118869.

Pasquini, J., Durcan, R., Wiblin, L., Stokholm, M.G., Rochester, L., Brooks, D.J., et al., 2019. Clinical implications of early caudate dysfunction in Parkinson's disease. J. Neurol. Neurosurg. Psychiatry 90 (10), 1098–1104. https://doi.org/10.1136/jnnp-2018-320157.

Peelle, J.E., Cusack, R., Henson, R.N.A., 2012. Adjusting for global effects in voxel-based morphometry: gray matter decline in normal aging. Neuroimage 60 (2), 1503–1516. https://doi.org/10.1016/j.neuroimage.2011.12.086.

Peters, S.M.B., van der Werf, N.R., Segbers, M., van Velden, F.H.P., Wierts, R., Blokland, K.J.A.K., et al., 2019. Towards standardization of absolute SPECT/CT quantification: a multi-center and multi-vendor phantom study. EJNMMI Phys. 6 (1), 29. https://doi.org/10.1186/s40658-019-0268-5.

Presotto, L., Iaccarino, L., Sala, A., Vanoli, E.G., Muscio, C., Nigri, A., et al., 2018b. Low-dose CT for the spatial normalization of PET images: a validation procedure for amyloid-PET semi-quantification. NeuroImage Clin. 20, 153–160. https://doi.org/10.1016/j.nicl.2018.07.013.

Reig, S., Penedo, M., Gispert, J.D., Pascau, J., Sánchez-González, J., García-Barreno, P., Desco, M., 2007. Impact of ventricular enlargement on the measurement of metabolic activity in spatially normalized PET. Neuroimage 35 (2), 748–758. https://doi.org/10.1016/j.neuroimage.2006.12.015.

Ridwan, A.R., Niaz, M.R., Wu, Y., Qi, X., Zhang, S., Kontzialis, M., et al., 2021. Development and evaluation of a high performance T1-weighted brain template for use in studies on older adults. Hum. Brain Mapp. 42 (6), 1758–1776. https://doi.org/10.1002/hbm.25327.

Rorden, C., Bonilha, L., Fridriksson, J., Bender, B., Karnath, H.O., 2012. Age-specific CT and MRI templates for spatial normalization. Neuroimage 61 (4), 957–965. https://doi.org/10.1016/j.neuroimage.2012.03.020.

Shattuck, D.W., Sandor-Leahy, S.R., Schaper, K.A., Rottenberg, D.A., Leahy, R.M., 2001. Magnetic resonance image tissue classification using a partial volume model. Neuroimage 13 (5), 856–876. https://doi.org/10.1006/nimg.2000.0730.

Xiong, Y., Ye, C., Chen, Y., Zhong, X., Chen, H., Sun, R., et al., 2022. Altered functional connectivity of basal ganglia in mild cognitive impairment and Alzheimer's disease. Brain Sci. 12 (11), 1555. https://doi.org/10.3390/brainsci12111555.

Yepes-Calderon, F., McComb, J.G., 2022. Accurate image-based CSF volume calculation of the lateral ventricles. Sci. Rep. 12 (1), 12115. https://doi.org/10.1038/s41598-022-15995-w.

Zhang, T., Wu, S., Zhang, X., Dai, Y., Wang, A., Zhang, H., Tian, M., 2022. Spatial normalization and quantification approaches of PET imaging for neurological disorders. Eur. J. Nucl. Med. Mol. Imaging 49 (11), 3809–3829. https://doi.org/10.1007/s00259-022-05809-6.